Microstructure Evolution and Mechanical Properties of Refractory Mo-Nb-V-W-Ti High-Entropy Alloys

Maximilian Regenberg *, Georg Hasemann *, Markus Wilke, Thorsten Halle and **Manja Krüger**

Institute of Materials and Joining Technology, Otto-von-Guericke University Magdeburg, Universitätsplatz 2, 39106 Magdeburg, Germany; markus.wilke@ovgu.de (M.W.); thorsten.halle@ovgu.de (T.H.); manja.krueger@ovgu.de (M.K.)

* Correspondence: maximilian.regenberg@ovgu.de (M.R.); georg1.hasemann@ovgu.de (G.H.); Tel.: +49-391-67-54572 (M.R.)

Abstract: High-entropy alloys can either be defined as solid solution alloys containing at least five elements in equiatomic or near-equiatomic composition, or as alloys with high configurational entropies (larger than 1.5R), regardless of the number of elements involved. The present study reports on an alloy design route for refractory high-entropy alloys based on equiatomic Mo-Nb-V alloys with additions of W and Ti. In general, the work was motivated by Senkov et al. The aim of the experiments carried out was to produce a refractory high-entropy alloy with a single-phase structure. For this purpose, a systematic alloy design involving four- and five-element compositions was used. Scanning electron microscopy analysis has shown that Mo-Nb-V-xW-yTi (x = 0, 20; y = 5, 10, 15, 20, 25) is in fact a refractory high-entropy alloy with a body-centered cubic dendritic structure. Furthermore, the Ti-concentration of the experimental alloys was varied, to obtain the influence of Titanium on the microstructure development. Additionally, compressive tests at room temperature were carried out to evaluate the influence of the different alloying elements and the Ti-fraction on the mechanical properties. The observations of the present work are then compared to the published results on similar alloys from the working group of Yao et al. and critically discussed.

Keywords: high-entropy alloys; refractory metals; microstructure; mechanical properties

1. Introduction

To meet the increasing demand for modern high-temperature materials, extensive research is being carried out in this field. Especially characteristics such as high-temperature strength, creep resistance and oxidation behavior are in the focus of present investigations. As the melting temperatures of materials correlate with the aforesaid properties, emphasis has been put on for example Fe, Ni or Pt and refractory elements like Mo and Nb, as basic alloying components in the manner of producing rather simple binary and ternary alloys, up to complex multi-component superalloys [1–4].

Besides the classical alloying strategies, starting from a base element and adding minor element additions to design and produce alloys, a multi-component alloy strategy offers the opportunity to design and investigate a completely new class of materials. In general, those alloys consist of five (or more) elements. They are referred to as high-entropy alloys (HEAs) if a single-phase material with relatively simple fcc (face-centered cubic), bcc (body centered cubic), or hcp (hexagonal close-packed) crystal structures is reached [5–8]. These, mostly equiatomic alloys, gained tremendous scientific attention, caused by their unique properties, such as high strength and hardness (even at high temperatures), outstanding wear resistance, good structural stability, corrosion and oxidation resistance. Those properties are attributed to certain interatomic and lattice effects: the core effect, high entropy

effect, sluggish diffusion effect, severe-lattice-distortion effect and a cocktail effect, which are described in detail elsewhere [5,8]. HEAs can be seen as a scientific approach to investigate and understand the metal–physical nature of this new type of materials.

A more practical (or engineering) approach on HEAs may lead to near-equiatomic multi-component alloys in which the element composition can vary in a certain compositional interval (between 5 at.% and 35 at.% as it is defined by Yeh [9]), for each principle element. As a result of that, it is possible to design so-called compositionally complex alloys (CCAs) which show the potential to lead to new developments regarding types of superalloys in which a multi-component solid solution matrix contains high amounts of complex precipitation phases [10–13].

During the last decade HEAs based on Fe, Al, Cr, Ni, Co, Cu and Mn were emphasized and extensively examined. A well-studied example of this development is Fe-Cr-Mn-Ni-Co [14–17], which is also known as the so-called Cantor alloy. To be noted in addition is the US Patent published by Bei [18] in which a multi-component solid solution alloy with high mixing entropy, namely Mo-Nb-V-W-Ti, has been mentioned. Senkov et al. [19,20] introduced HEAs based primarily on refractory metals (RHEAs) in demand for high- and ultra-high-temperature structural materials, i.e., in the aerospace industry. Their alloys based on W-Nb-Mo-Ta and W-Nb-Mo-Ta-V were experimentally investigated and have a dendritic bcc structure, which, compared to the Ni-based alloy Inconel 718, shows relatively high yield stresses in a wide temperature range between 600 °C and 1600 °C [20]. These observations lead to the assumption, that the patented alloy Mo-Nb-V-W-Ti also consists of a single-phase body-centered cubic structure. Senkov et al.'s alloys, however, have relatively high densities of 12.36 g/cm^3 for W-Nb-Mo-Ta and 13.75 g/cm^3 for W-Nb-Mo-Ta-V [19].

In general, the present work aims to follow Senkov et al.'s approach of developing an RHEA, based on principle refractory metals but by substituting at least one and/or both of the heavy elements W and Ta with Ti, to reduce the density of the RHEAs significantly. Thus, the alloying strategy of the present work is based on theoretical calculations which give rise to a stable solid solution formation. In addition, the effects of removing/substituting aforesaid elements on the strength and ductility of the alloys at room temperature was examined.

2. Materials and Methods

For the alloy design of the present study, three quaternary alloys $Mo_{25}Nb_{25}V_{25}W_{25}$, $Mo_{25}Nb_{25}V_{25}Ti_{25}$, $Mo_{30}Nb_{30}V_{30}Ti_{10}$ and two quinary alloys $Mo_{20}Nb_{20}V_{20}W_{20}Ti_{20}$, $Mo_{22.5}Nb_{22.5}V_{22.5}W_{22.5}Ti_{10}$ were chosen (all concentrations are given in atomic percent). The alloys were prepared from high-purity metal chips, granules and powders via arc-melting under protective (Ar) atmosphere (Arc Melter MAM-1, Edmund Buehler GmbH, Bodelshausen, Germany). Button-shaped samples of 5–10 g were re-melted and flipped five times each, to ensure good homogeneity.

Powder samples of the alloys produced were manually prepared for X-ray diffraction analysis (XRD, X'Pert PRO, Malvern Panalytival B.V., Almelo, The Netherlands), using a hand file. The measuring parameters chosen for the XRD analysis were Cu-Kα_1-radiation (λ = 1.541874 Å) at a voltage of 40 kV, current intensity of 30 mA and increment size of 0.0167°.

In order to characterize the as-cast microstructure, the button-shaped samples of each alloy were cut and prepared for metallographic examination. After initial grinding, the specimens were polished using a 3 μm and a 1 μm diamond suspension, and finally polished with colloidal silica (OP-S, Struers, Ballerup, Denmark). The microstructural observations were carried out using a scanning electron microscope (SEM) (ESEM XL30 FEG, FEI, Hillsboro, OR, USA). Additionally, to validate the chemical composition of the alloy samples, (Si(Li))-detector Energy-dispersive X-ray spectroscopy (EDS) analysis, equipped with Genesis software (EDAX, Mahwah, NJ, USA) was conducted. Moreover, area fractions of the microstructures of the Ti-containing 5-element alloys $Mo_{20}Nb_{20}V_{20}W_{20}Ti_{20}$ and $Mo_{22.5}Nb_{22.5}V_{22.5}W_{22.5}Ti_{10}$ were calculated by means of graphical image analysis (Photoshop, Adobe, San José, CA, USA) using 15 images each.

Furthermore, Vickers hardness measurements with an applied force of 100 N were performed on the prepared specimens, using a hardness testing device (Duravision, Struers, Ballerup, Denmark).

Regarding the compression tests, 3 to 4 cylindrical samples conforming to standards [21] with specifications of 3 mm in length and 1.8 mm in diameter were prepared by electric discharge machining (EDM). The samples were surface-cleaned (removal of a burr and the surface tarnish) subsequently afterwards, using 800 and 1200 grit SiC paper. The compression tests were performed on an electro-mechanical universal testing machine (TIRAtest 2825, TIRA GmbH, Schalkau, Germany) at a constant crosshead speed corresponding to an initial (engineering) strain rate of $\dot{\varepsilon} = 10^{-3} \text{ s}^{-1}$, up to a maximum deformation of ~50%. The yield strength was determined by the 0.2% offset method and the plastic strain was obtained by subtracting the combined compliance of the testing machine and the sample from the individually measured load-displacement curves.

3. Results and Discussion

3.1. Alloy Design Based on Thermodynamics and Geometrical Effects

The formation of a solid solution phase in multi-component alloys is determined by the system's Gibbs free energy ΔG_{mix} [22],

$$\Delta G_{\text{mix}} = \Delta H_{\text{mix}} - T\Delta S_{\text{mix}} \tag{1}$$

Hence, the phase formation in RHEAs is strongly dependent upon the interplay between the entropy of mixing ΔS_{mix}, the absolute temperature T and the enthalpy of mixing ΔH_{mix} [5]. Therefore, the following equations were used to determine the phase stability of the alloys examined [15,16]:

$$\Delta S_{\text{mix}} = -R \sum_{i=1}^{N} x_i \ln x_j \tag{2}$$

$$\Delta H_{\text{mix}} = \sum_{i=1;\ i\neq j}^{N} 4\Delta H_{\text{AB}}^{\text{mix}} x_i x_j \tag{3}$$

where, R is the gas constant, 8.314 J·mol^{-1}·K^{-1}, N is the number of elements, x_i or x_j is the composition of the ith or jth element and $\Delta H_{\text{AB}}^{\text{mix}}$ is the enthalpy of mixing for the binary equiatomic AB alloys. Furthermore, the ratio of entropy to enthalpy Ω (also referred to as solid solution prediction parameter) was used to make predictions about solid solution formation in the present alloying systems [23]:

$$\Omega = \frac{\sum_{i=1}^{n} c_i (T_{\text{m}})_i \Delta S_{\text{mix}}}{|\Delta H_{\text{mix}}|} \tag{4}$$

here, the melting temperature of an n-element alloy is calculated, where T_{m} is used as the melting point of the ith component of the alloy. Additionally, the atomic size difference δ_r in % was taken into account, using the equation given below [24]:

$$\delta_r\% = 100\% \sqrt{\sum_{i=1}^{n} c_i \left(1 - \frac{r_i}{\bar{r}}\right)^2} \tag{5}$$

where, C_i is the atomic fraction of the ith component, $\bar{r} = \sum_{i=1}^{n} c_i r_i$ is the average atomic radius and r_i is the atomic radius (listed in reference [25]).

The results of the calculations performed (as displayed in Table 1) are in good agreement with the findings of Zhang et al. [26,27], stating that low values of ΔH_{mix} and, respectively, high values of ΔS_{mix} reduce the free energy of the system, thus providing a stable solid solution phase. This assumption is supported by the Ω values stated, all of which are significantly higher than 1 ($\Omega_{\text{min}} = \Omega(\text{Mo}_{25}\text{Nb}_{25}\text{V}_{25}\text{W}_{25}) = 8.27$), leading to a more dominant contribution of $(T)\Delta S_{\text{mix}}$ than of ΔH_{mix} to the free energy of the system [23]. In addition to the entropy of mixing, the δ_r data of the elements mixed contribute to the formation of phases, since the lattice distortion is influenced

by the different atomic radii [28]. The stated RHEA alloys show δ_r values between 2.98% and 4.62%, hence indicating the formation of a stable solid solution [29].

Table 1. Investigated alloys, and calculated values for the entropy of mixing ΔS_{mix}, the enthalpy of mixing ΔH_{mix}, the solid solution prediction parameter Ω and the atomic size difference δ_r.

Alloy	ΔS_{mix}, J·K^{-1}·mol^{-1}	ΔH_{mix}, kJ·mol^{-1}	Ω	δ_r, %
$Mo_{25}Nb_{25}V_{25}W_{25}$	11.52	−4.00	8.27	2.98
$Mo_{25}Nb_{25}V_{25}Ti_{25}$	11.52	−2.75	10.20	4.46
$Mo_{30}Nb_{30}V_{30}Ti_{10}$	10.92	−3.00	9.23	4.01
$Mo_{20}Nb_{20}V_{20}W_{20}Ti_{20}$	13.38	−4.16	8.63	4.05
$Mo_{22.5}Nb_{22.5}V_{22.5}W_{22.5}Ti_{10}$	13.08	−4.14	8.77	3.65

To demonstrate and evaluate the potential of the alloys examined, the generated ΔH_{mix} vs. δ_r data were graphically displayed in Figure 1a by means of a field diagram, showing the regions of theoretical solid solution, respectively, amorphous phase formation, and compared to obtained data from the corresponding literature.
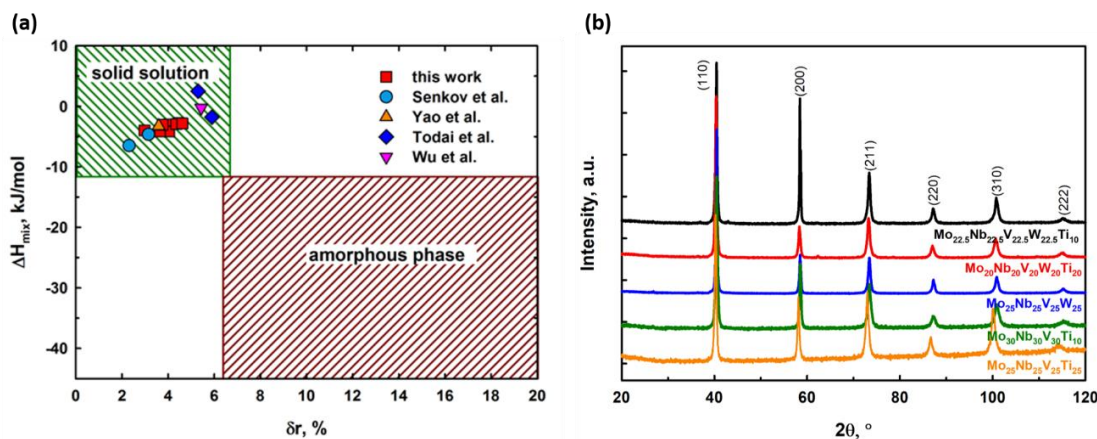

Figure 1. (**a**) Calculated ΔH_{mix} to δ_r ratios from the present work compared to data, obtained from the corresponding literature [26,27]. (**b**) XRD patterns of the alloys examined in the as-cast condition (from top to bottom).

3.2. X-ray Diffraction of the RHEAs

The XRD analysis results of the RHEA powder samples are depicted in patterns, displaying the relative intensity of the detected reflexes over a 2-θ-range from 20° to 120° in Figure 1b. The XRD reflexes of the different alloys show similar locations, indicating the presence of a bcc crystal structure in all alloys examined. The positions of the diffraction reflexes present are characteristic for elements with a bcc crystal structure (f.e. the refractory elements Mo, V, Nb, W, etc.) in general, however they are slightly shifted here [30]. The exact position of the reflexes obtained varies, due to the lattice distortion of the different solid solutions. The experimentally obtained lattice parameters reaching from a minimum of 3.156 Å ($Mo_{22.5}Nb_{22.5}V_{22.5}W_{22.5}Ti_{10}$) to a maximum value of 3.174 Å ($Mo_{25}Nb_{25}V_{25}Ti_{25}$) are listed in Table 2. Theoretical values for the alloys examined were determined, using the equation [19]:

$$a_{theor.} = \sum c_i a_i \tag{6}$$

and the results, stated in Table 2 are in good agreement with the experimental values.

Table 2. Theoretically calculated and experimentally measured lattice parameters of the alloys investigated with standard deviations.

Alloy	Theor. Lattice Parameter, Å	Exp. Lattice Parameter, Å	Deviation
$Mo_{25}Nb_{25}V_{25}W_{25}$	3.160	3.157	±0.11
$Mo_{25}Nb_{25}V_{25}Ti_{25}$	3.196	3.174	±0.009
$Mo_{30}Nb_{30}V_{30}Ti_{10}$	3.173	3.156	±0.002
$Mo_{20}Nb_{20}V_{20}W_{20}Ti_{20}$	3.189	3.164	±0.013
$Mo_{22.5}Nb_{22.5}V_{22.5}W_{22.5}Ti_{10}$	3.175	3.159	±0.008

3.3. As-Cast Microstructures of the Alloys Examined

As-cast microstructure overview-images of the five alloys produced are depicted in Figure 2. The images were taken at a central position of the arc-melted buttons. In addition, the results of the chemical compositions, analyzed by means of EDS, are shown in Table 3. It can be stated that the actual element concentration is in good agreement with the theoretical calculated values, with a maximum deviation of ±2.1 at.% W in alloy $Mo_{20}Nb_{20}V_{20}W_{20}Ti_{20}$, regarding all alloys tested. The microstructure evolution is of a similar kind within the button-shaped samples. In principal, the formation of dendrites in different sizes and refinement can be examined. As displayed on alloy $Mo_{25}Nb_{25}V_{25}W_{25}$ in Figure 3, a coarse-grained dendritic structure is present in the bottom regions of the button-shaped samples, while a more distinctive growth can be obtained from the mid to the top section of the samples. This is attributed to the cooling conditions in the arc-melter or more specifically the fast heat transfer from the sample into the water-cooled copper crucible, thus restricting the dendrite growth.

Even though theory predicts the formation of a solid solution, regarding the Ti-containing 5-element alloys, the presence of a second phase was observed at higher magnifications (small, black colored areas), which are depicted in the micrograph insets of the EDS element mappings. The EDS analysis (Figure 4) revealed that these areas are indeed Ti-rich precipitations, which form at the grain boundaries of the dendrites during solidification (~5% area fraction in alloy $Mo_{22.5}Nb_{22.5}V_{22.5}W_{22.5}Ti_{10}$ and ~7% area fraction in alloy $Mo_{20}Nb_{20}V_{20}W_{20}Ti_{20}$). The reason for the formation of the dendritic microstructure in general and the Ti-precipitations in particular lies within the different melting temperatures of the elements present. As titanium exhibits the lowest melting temperature ($T_m \approx 1660\ °C$) of the alloying elements used, hence solidifying last, the solidification front is pushing the low viscous residual melt forward, resulting in a Ti-enriched interdendritic zone [31]. This observation can also be expanded to vanadium, which exhibits the second lowest melting temperature ($T_m \approx 1910\ °C$), thus experiencing the same influence (depicted in the EDS mappings in Figure 4). Depending on the alloy composition, tungsten ($T_m \approx 3420\ °C$), molybdenum ($T_m \approx 2620\ °C$) and niobium ($T_m \approx 2480\ °C$) constitute the dendritic crystals, respectively, suppressing the remaining alloying elements in the interdendritic region. If W is present in the alloy (cf. the five-component alloy (Figure 4b), the primary dendrites mainly consist of it, which is due to the extremely high melting point. If the alloy only contains Mo and Nb instead of W as high melting components (cf. the four-element alloy (Figure 4a), the primary dendrites are enriched with both of the aforesaid elements, which can be attributed to the more similar meting point of the components. The results of the EDS mappings were quantitatively verified by means of spot analysis in the dendritic (C_d), interdendritic (C_{id}) and precipitation (C_{pr}) regions of the samples (examples regarding alloy $Mo_{25}Nb_{25}V_{25}Ti_{25}$ and $Mo_{20}Nb_{20}V_{20}W_{20}Ti_{20}$ are listed in Table 4) and are overall in good agreement.

Table 3. Chemical compositions (at.%) of the alloys investigated with standard deviations, determined by EDS analysis.

Alloy	Mo	V	Nb	W	Ti
$Mo_{25}Nb_{25}V_{25}W_{25}$	28 ± 1	21 ± 1	26 ± 1	25 ± 2	-
$Mo_{25}Nb_{25}V_{25}Ti_{25}$	26 ± 1	24 ± 0.1	26 ± 0.1	-	24 ± 1
$Mo_{30}Nb_{30}V_{30}Ti_{10}$	31 ± 0.1	28 ± 0.1	31 ± 0.1	-	10 ± 0.2
$Mo_{20}Nb_{20}V_{20}W_{20}Ti_{20}$	21 ± 1	19 ± 1	21 ± 0.4	20 ± 2	19 ± 1
$Mo_{22.5}Nb_{22.5}V_{22.5}W_{22.5}Ti_{10}$	26 ± 1	23 ± 0.2	22 ± 0.2	20 ± 0.2	10 ± 0.1
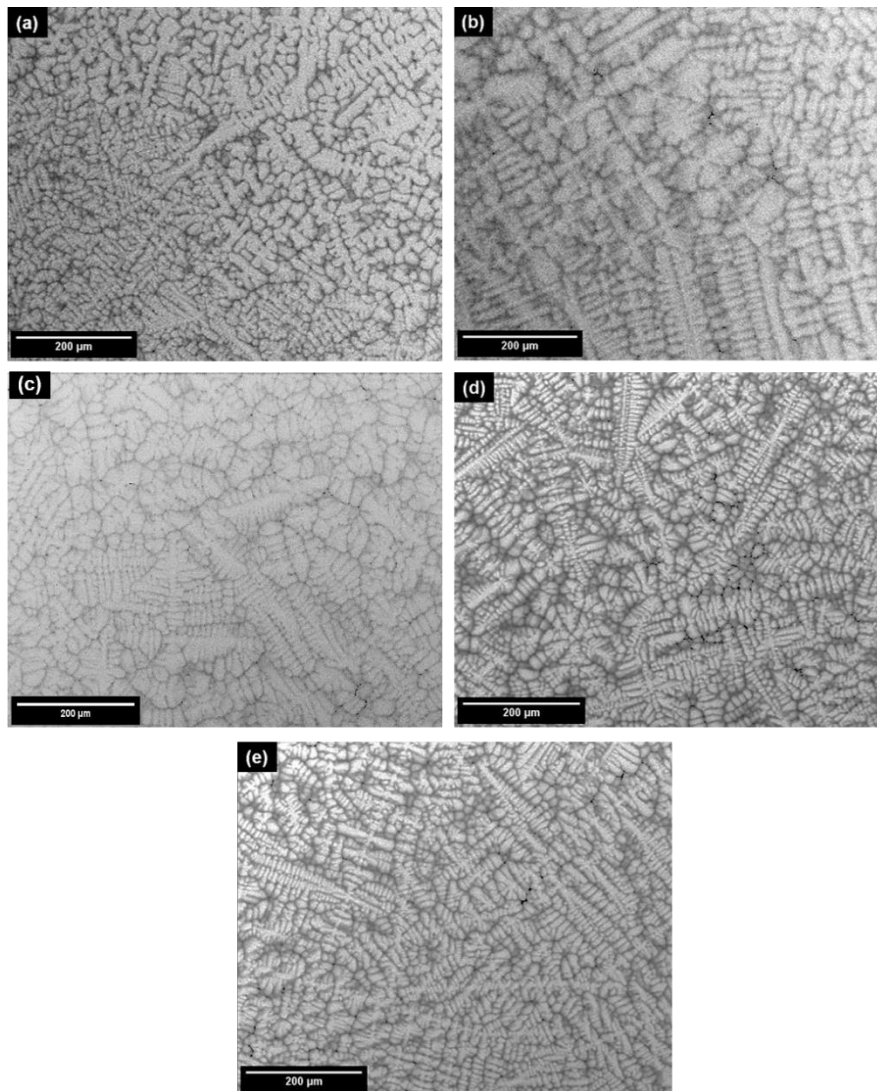
Figure 2. SEM backscattered electron (BSE) overview-images of the as-cast microstructures of $Mo_{25}Nb_{25}V_{25}W_{25}$ (**a**), $Mo_{25}Nb_{25}V_{25}Ti_{25}$ (**b**), $Mo_{30}Nb_{30}V_{30}Ti_{10}$ (**c**), $Mo_{20}Nb_{20}V_{20}W_{20}Ti_{20}$ (**d**) and $Mo_{22.5}Nb_{22.5}V_{22.5}W_{22.5}Ti_{10}$ (**e**).
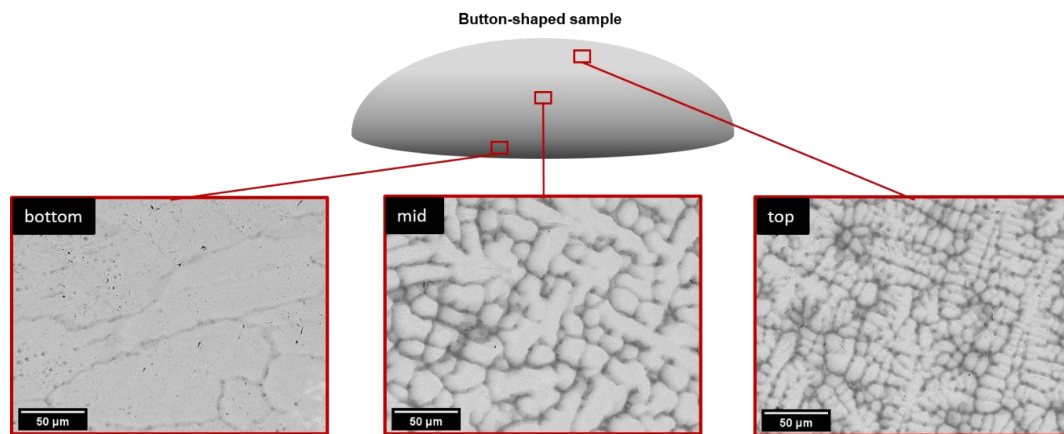
Figure 3. Microstructural differences in the formation of dendrites across the produced button-shaped samples, exemplified on alloy $Mo_{25}Nb_{25}V_{25}W_{25}$.
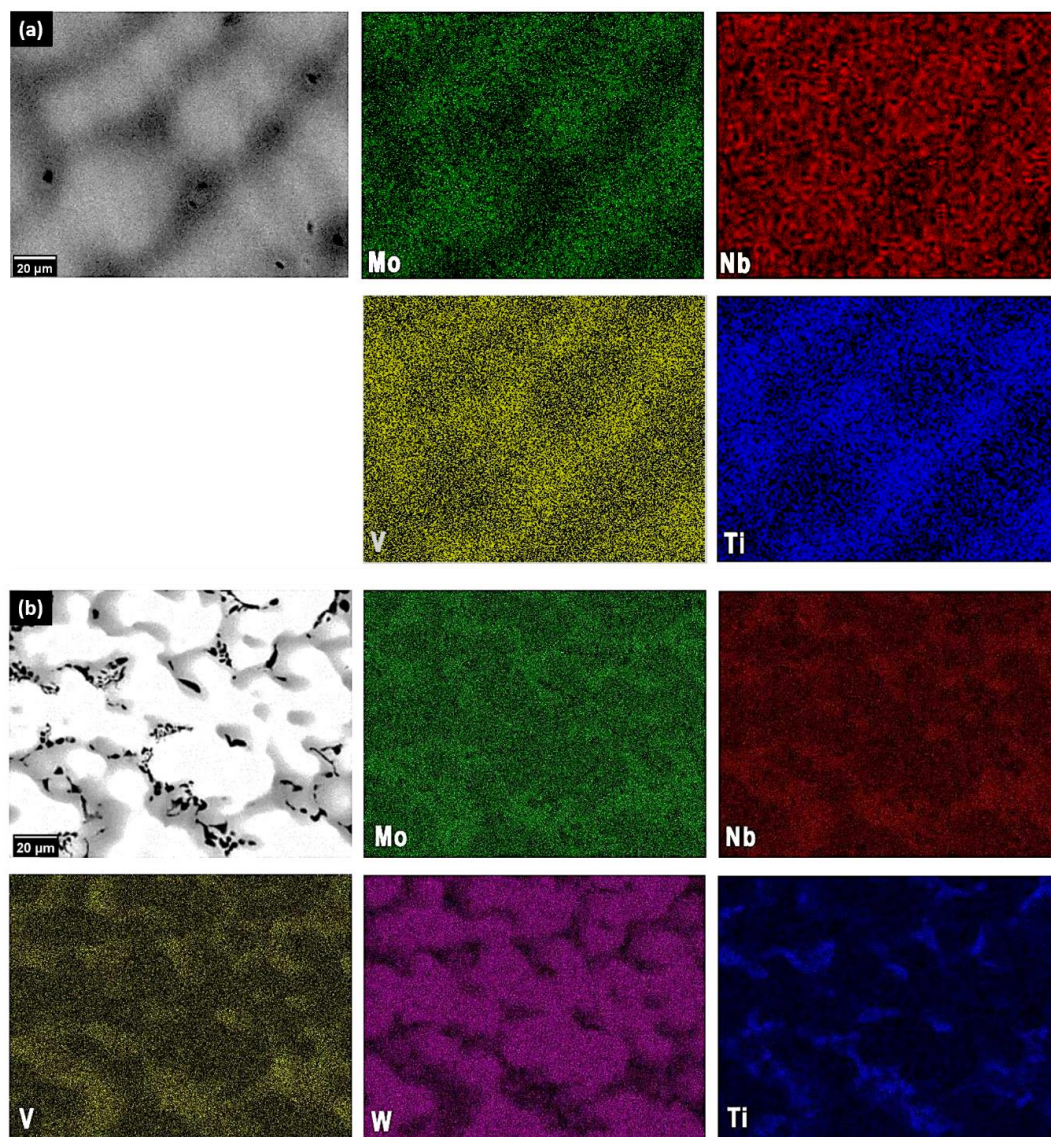
Figure 4. EDS mappings of the refractory high-entropy alloys (RHEAs) $Mo_{25}Nb_{25}V_{25}Ti_{25}$ (**a**) and $Mo_{20}Nb_{20}V_{20}W_{20}Ti_{20}$ (**b**).

Table 4. Results of the EDS spot analysis in the dendritic (C_d), interdendritic (C_{id}), and precipitation (C_{pr}) areas of alloy $Mo_{25}Nb_{25}V_{25}Ti_{25}$ and alloy $Mo_{20}Nb_{20}V_{20}W_{20}Ti_{20}$.

Alloy	Area	Mo, at.%	Nb, at.%	V, at.%	W, at.%	Ti, at.%
$Mo_{25}Nb_{25}V_{25}Ti_{25}$	C_d	28	28	22	-	22
	C_{id}	16	22	31	-	30
$Mo_{20}Nb_{20}V_{20}W_{20}Ti_{20}$	C_d	23	19	14	32	12
	C_{id}	19	25	26	11	19
	C_{pr}	2	7	5	2	85

3.4. Mechanical Properties at Room Temperature

The results of the compression tests regarding the obtained compressive yield strength values (yield strength in the following) vs. the theoretical density of the samples, determined by the formula to calculate the density of a disordered solid solution [19]:

$$\rho_{\text{theor.}} = \frac{\sum c_i A_i}{\sum \frac{c_i A_i}{\rho_i}}, \tag{7}$$

are displayed in Figure 5a. In addition, the obtained hardness values of the RHEAs vs. the theoretical density are depicted in Figure 5b. The corresponding numerical values as well as the calculated theoretical densities of the alloys examined are stated in Table 5. Overall, the alloys tested show relatively high yield strength and low ductility values, which is attributed to the large valence electron concentration (VEC) [8,32] and are in good agreement with the findings of Senkov et al. [19,20]. Nonetheless, it must be stated that the values considering the compressive yield stress partly show some major deviations which is attributed to the presence of porosity in the compression samples. This originates mainly in the manufacturing process. As the specimens were produced by means of arc melting, process related porosity could not be prevented. The ultra-high melting points of the elements used complicate the melting process, leading to a highly viscous melt which solidifies quickly, thus resulting in the present gas porosity and cavities. Referring to the samples of alloy $Mo_{22.5}Nb_{22.5}V_{22.5}W_{22.5}Ti_{10}$, the obtained porosity is so significant that it can be determined as the main failure mechanism, thus the results of alloy $Mo_{22.5}Nb_{22.5}V_{22.5}W_{22.5}Ti_{10}$ were not taken into account and are therefore not displayed in the images. By comparing the depicted graphs, it is noticeable that there is no linear dependency present between the yield strength and the theoretical density of the alloys in contrast to the measured hardness values and the theoretical density. The yield strength values of the alloys $Mo_{25}Nb_{25}V_{25}Ti_{25}$, $Mo_{20}Nb_{20}V_{20}W_{20}Ti_{20}$ and $Mo_{25}Nb_{25}V_{25}W_{25}$ are comparable, while alloy $Mo_{30}Nb_{30}V_{30}Ti_{10}$ displays the highest value. This observation leads to the assumption that a reduced Ti-content (10 at.% in alloy $Mo_{30}Nb_{30}V_{30}Ti_{10}$ vs. 25 at.% in alloy $Mo_{25}Nb_{25}V_{25}Ti_{25}$ and 20 at.% in alloy $Mo_{20}Nb_{20}V_{20}W_{20}Ti_{20}$), respectively, and higher content of the elements Mo, Nb and V, results in a higher compressive yield strength. By showing a relatively low yield strength, however, alloy $Mo_{25}Nb_{25}V_{25}W_{25}$ is in contrast to this statement. On the one hand, this can be attributed to the aforementioned porosity in the $Mo_{25}Nb_{25}V_{25}W_{25}$ specimens. On the other hand, the high W (25 at.% W) concentration in the alloy leads to lower concentrations of the strength enhancing components Mo, Nb and V (compared to alloy $Mo_{30}Nb_{30}V_{30}Ti_{10}$ f.e.) and the enrichment of W in the dendritic crystals must be considered. This results in a suppression of the lower-melting elements in the interdendritic regions, hence generating an imbalance in the element distribution.
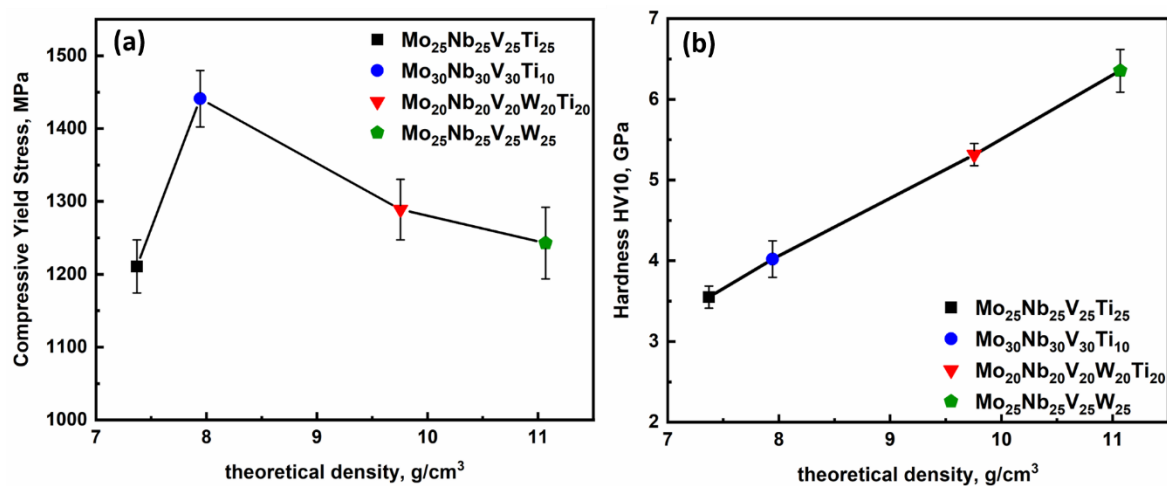
Figure 5. Compressive Yield Stress—theoretical density curve (**a**) and hardness—theoretical density curve (**b**) of the alloys investigated.

Table 5. Theoretical densities of the present HEAs in increasing order, as well as the obtained compressive yield stress values, the specific compressive yield stress values and the hardness values.

Alloy	$\rho_{theor.}$, g·cm^{-3}	$\sigma_{0.2}$, MPa	$\sigma_{0.2\ spec.}$, MPa·cm^3/g	Hardness HV10, GPa
$Mo_{25}Nb_{25}V_{25}Ti_{25}$	7.4	1210 ± 36	164 ± 5	4 ± 0.1
$Mo_{30}Nb_{30}V_{30}Ti_{10}$	7.9	1441 ± 39	182 ± 5	4 ± 0.2
$Mo_{20}Nb_{20}V_{20}W_{20}Ti_{20}$	9.8	1289 ± 42	132 ± 4	5 ± 0.1
$Mo_{25}Nb_{25}V_{25}W_{25}$	11.1	1243 ± 49	112 ± 4	6 ± 0.2

Regarding the macro-hardness of the samples and the density, a clear connection between the alloying elements can be obtained. Alloy $Mo_{25}Nb_{25}V_{25}Ti_{25}$ displays the lowest HV10 value as well as the lowest density, due to the high fraction of Ti. With decreasing Ti content in relation to the other alloying elements, the hardness of the microstructure increases in correlation with the density. A significant increase (both in hardness and density) can be examined regarding the alloys $Mo_{20}Nb_{20}V_{20}W_{20}Ti_{20}$ and $Mo_{25}Nb_{25}V_{25}W_{25}$, respectively, which is attributed to the addition of W [19]. Compared to Mo-Nb-V-Ta-Ti alloys investigated by Bei et al. [18] the present results are in good agreement with their hardness values. Thus, substituting W with Ta reveals similar mechanical properties in combination with a decreased density and melting point of the alloy.

In order to position the yield strength in relation to the density (hence the W fraction as it affects the alloys examined the most), the specific compressive yield strengths (SCYS) of the alloys tested were calculated (Table 5). The calculated values were then compared to the obtained compressive yield stresses and displayed in Figure 6. The graph clearly demonstrates the influence of the light elements (mainly Ti, but also V), respectively, the heavy element (W) in the alloy composition: Alloy $Mo_{25}Nb_{25}V_{25}Ti_{25}$ exhibits a major gap between the two values, which is attributed to the proportionally high Ti and V content, resulting in a comparatively high SCYS. Alloy $Mo_{30}Nb_{30}V_{30}Ti_{10}$ also shows a, however smaller, increase in the SCYS which still is the highest value overall (due to the aforementioned high fractions of Mo and Nb). In contrast to the alloys discussed, alloy $Mo_{20}Nb_{20}V_{20}W_{20}Ti_{20}$ and alloy $Mo_{25}Nb_{25}V_{25}W_{25}$ show a decrease in SCYS in relation to the obtained compressive yield stress, primarily caused by the increased density of both alloys, thus putting the actual increase in the compressive yield stress into perspective. Comparing the SCYS values of all alloys it can be stated that an approximation to a linear trend is present (in contrast to the compressive yield stress values), which leads to an interesting perspective and more faceted way of comparing the microstructure evolution and the resulting properties of RHEAs such as the ones investigated.
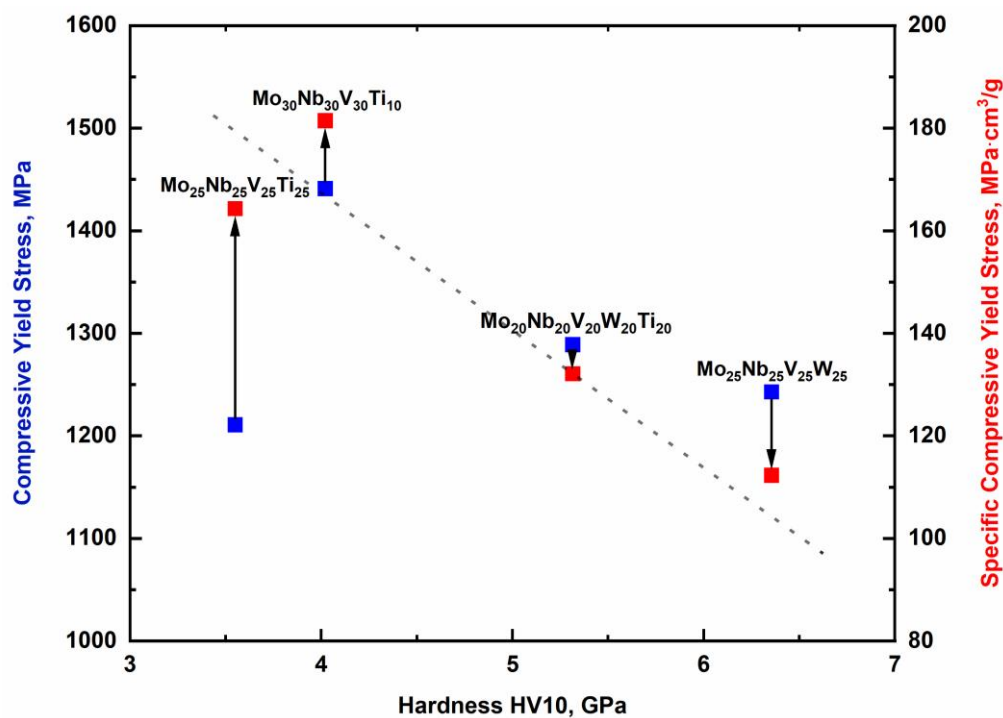
Figure 6. Comparison of compressive yield stress and specific compressive yield stress with respect to the hardness of the alloys tested.

3.5. Comparison with Other Works and Superalloys

A comparison regarding SCYS vs. the hardness of different RHEAs, which were the focus of published research in recent years by Yao et al. [33,34] and Senkov et al. [20], common Ni-based superalloys Inconel 718 [35], alloy CMSX-4 [36,37] and alloy Haynes 282 [38] and the alloys investigated in this work is displayed in Figure 7. Considering the SCYS and the hardness values, the examined alloys are superior in comparison to the superalloys. Only alloy $Mo_{25}Nb_{25}V_{25}W_{25}$ shows a lower SCYS, compared to alloy Inconel 718, however the hardness is significantly higher. In general, the examined alloys fit in well with the values obtained from the other RHEAs. The Ti-containing alloys $Mo_{25}Nb_{25}V_{25}Ti_{25}$ and $Mo_{30}Nb_{30}V_{30}Ti_{10}$ show the highest SCYS values of all alloys depicted, which can be attributed to the high Ti and V fractions, thus showing reduced density, compared with the Ta containing alloys from Yao et al. [33,34]. In comparison, the high W-containing alloy $Mo_{25}Nb_{25}V_{25}W_{25}$ has the lowest SCYS but highest hardness values of the alloys investigated in this study, similar to alloy $Mo_{20}Nb_{20}V_{20}W_{20}Ta_{20}$ by Senkov et al. [20]. Thus, the alloy $Mo_{20}Nb_{20}V_{20}W_{20}Ti_{20}$ represents a good compromise between strength and hardness which seems to agree with similar alloy compositions investigated by Yao et al. [33,34].
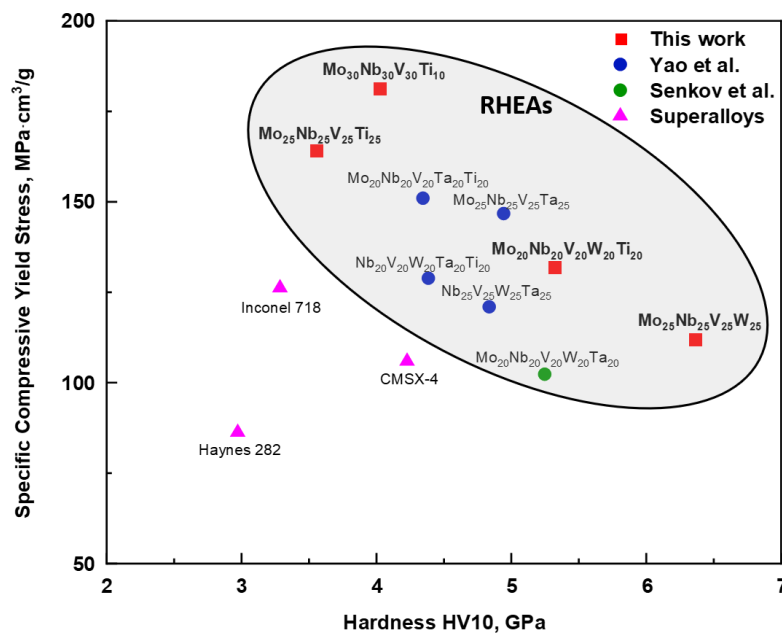
Figure 7. Specific compressive yield stress and hardness of different RHEAs, investigated by Yao et al. [33,34] and Senkov et al. [20], common Ni-based superalloys [35–38] and the alloys examined in this work for comparison.

4. Conclusions

The microstructure evolution and mechanical properties of RHEA alloys $Mo_{25}Nb_{25}V_{25}W_{25}$, $Mo_{25}Nb_{25}V_{25}Ti_{25}$, $Mo_{30}Nb_{30}V_{30}Ti_{10}$, $Mo_{20}Nb_{20}V_{20}W_{20}Ti_{20}$ and $Mo_{22.5}Nb_{22.5}V_{22.5}W_{22.5}Ti_{10}$ were investigated in the present work.

The alloy design was based on thermodynamic calculations regarding the Gibbs free energy ΔG_{mix}, the entropy of mixing ΔS_{mix}, the enthalpy of mixing ΔH_{mix} and the solid solution prediction parameter Ω, as well as geometrical effects, considering the difference of atomic radii δ_r.

XRD analysis showed that all alloys examined have a bcc crystal structure with a lattice parameter between 3.156 Å ($Mo_{22.5}Nb_{22.5}V_{22.5}W_{22.5}Ti_{10}$) and 3.174 Å ($Mo_{25}Nb_{25}V_{25}Ti_{25}$), however, the presence of a second, Ti-enriched phase could be detected subsequently via SEM observations. The second phase was not distinguished by the XRD method (no shoulders or modifications of the reflexes as such were determined) due to the small volume fractions present.

Microstructure analysis demonstrated that the alloys produced show a similar single-phase dendritic structure, apart from aforementioned alloy $Mo_{20}Nb_{20}V_{20}W_{20}Ti_{20}$ and alloy $Mo_{22.5}Nb_{22.5}V_{22.5}W_{22.5}Ti_{10}$. Deviations in the microstructure-refinement of the different samples were also obtained, which could be attributed to the cooling conditions during the arc-melting process.

To verify the composition of the samples, EDS spot analysis and mappings were conducted, which showed a good distribution of the alloying elements overall and an enrichment of high melting elements in the dendrite crystals vs. an accumulation of elements with a lower melting temperature in the interdendritic regions.

The mechanical properties of the alloys were obtained by means of room temperature compression tests and macro-hardness measurements, which revealed various impacts of the elements involved. The compressive yield strength of the alloys tested is mainly influenced by the Mo and Nb fraction present (see f.e. alloy $Mo_{30}Nb_{30}V_{30}Ti_{10}$: $\sigma_{0.2} = 1440 \pm 40$ MPa vs. alloy $Mo_{25}Nb_{25}V_{25}Ti_{25}$: $\sigma_{0.2} = 1210 \pm 36$ MPa). The W fraction primarily influences the hardness of the alloys; nonetheless, an impact on the compressive yield stress can be obtained regarding alloy $Mo_{20}Nb_{20}V_{20}W_{20}Ti_{20}$. The density of the Alloys examined was primarily determined by Ti, V and W (see alloy $Mo_{25}Nb_{25}V_{25}Ti_{25}$: highest share of Ti and V, lowest density vs. alloy $Mo_{25}Nb_{25}V_{25}W_{25}$: highest share of W, highest density). At this point, the determined porosity which was mainly caused

by the arc-melting process as such and the highly viscous melt should also be noted. A different melting process (f.e. cold crucible induction melting) as well as the selection of lower-melting elements shall be mentioned here as alternatives for samples with reduced porosity/cavities.

Additionally, a comparison between the specific compressive yield strength and the nominal compressive yield strength has been carried out, which led to a more differentiated relation between the density (respectively, the content of light elements) and the compressive yield stress vs. the hardness of the alloys investigated. The calculated specific compressive yield stress values were finally compared to other RHEAs and Ni-base superalloys by means of a scatter diagram.

Author Contributions: Conceptualization, M.K., T.H. and G.H.; methodology, M.R., G.H. and M.W.; validation, G.H. and M.K.; formal analysis, M.R., G.H., M.W., T.H. and M.K.; investigation, M.R., G.H. and M.W.; writing—original draft preparation, M.R.; writing—review and editing; M.R., G.H. and M.K.; supervision, M.K. and T.H., funding acquisition, M.K. and T.H. All authors have read and agreed to the published version of the manuscript.

Conflicts of Interest: The authors declare no conflict of interest.

References

1. Speich, G.R.; Schwoeble, A.J.; Leslie, W.C. Elastic constants of binary iron-base alloys. *Metall. Trans.* **1972**, *3*, 2031–2037. [CrossRef]
2. Tawancy, H.M.; Klarstrom, D.L.; Rothman, M.F. Development of a New Nickel-Base Superalloy. *JOM* **1984**, *36*, 58–62. [CrossRef]
3. Hemmersmeier, U.; Feller-Kniepmeier, M. Element distribution in the macro- and microstructure of nickel base superalloy CMSX-4. *Mater. Sci. Eng. A* **1998**, *248*, 87–97. [CrossRef]
4. Dimiduk, D.M.; Perepezko, J.H. Mo-Si-B alloys: Developing a revolutionary turbine-engine material. *MRS Bull.* **2003**, *28*, 639–645. [CrossRef]
5. Gao, M.C.; Liaw, P.K.; Yeh, J.W.; Zhang, Y. *High-Entropy Alloys: Fundamentals and Applications*; Springer International Publishing: Basel, Switzerland, 2016; ISBN 9783319270135.
6. Yeh, J.W. Alloy design strategies and future trends in high-entropy alloys. *JOM* **2013**, *65*, 1759–1771. [CrossRef]
7. George, E.P.; Raabe, D.; Ritchie, R.O. High-entropy alloys. *Nat. Rev. Mater.* **2019**, *4*, 515–534. [CrossRef]
8. George, E.P.; Curtin, W.A.; Tasan, C.C. High entropy alloys: A focused review of mechanical properties and deformation mechanisms. *Acta Mater.* **2020**, *188*, 435–474. [CrossRef]
9. Tsai, M.H.; Yeh, J.W. High-entropy alloys: A critical review. *Mater. Res. Lett.* **2014**, *2*, 107–123. [CrossRef]
10. Manzoni, A.; Daoud, H.; Mondal, S.; Van Smaalen, S.; Völkl, R.; Glatzel, U.; Wanderka, N. Investigation of phases in Al23Co15Cr 23Cu8Fe15Ni16 and Al 8Co17Cr17Cu8Fe17Ni 33 high entropy alloys and comparison with equilibrium phases predicted by Thermo-Calc. *J. Alloys Compd.* **2013**, *552*, 430–436. [CrossRef]
11. Manzoni, A.M.; Daoud, H.M.; Voelkl, R.; Glatzel, U.; Wanderka, N. Influence of W, Mo and Ti trace elements on the phase separation in Al8Co17Cr17Cu8Fe17Ni33 based high entropy alloy. *Ultramicroscopy* **2015**, *159*, 265–271. [CrossRef]
12. Manzoni, A.M.; Singh, S.; Daoud, H.M.; Popp, R.; Völkl, R.; Glatzel, U.; Wanderka, N. On the path to optimizing the Al-Co-Cr-Cu-Fe-Ni-Ti high entropy alloy family for high temperature applications. *Entropy* **2016**, *18*, 104. [CrossRef]
13. Bolbut, V.; Wessel, E.; Krüger, M. Phase stability and temperature-dependent compressive strength of a low-density Fe32.3Al29.3Cu11.7Ni10.8Ti15.9 alloy. *Scr. Mater.* **2018**, *150*, 54–56. [CrossRef]
14. Cantor, B.; Chang, I.T.H.; Knight, P.; Vincent, A.J.B. Microstructural development in equiatomic multicomponent alloys. *Mater. Sci. Eng. A* **2004**, *375–377*, 213–218. [CrossRef]
15. Yeh, J.W.; Chen, S.K.; Lin, S.J.; Gan, J.Y.; Chin, T.S.; Shun, T.T.; Tsau, C.H.; Chang, S.Y. Nanostructured high-entropy alloys with multiple principal elements: Novel alloy design concepts and outcomes. *Adv. Eng. Mater.* **2004**, *6*, 299–303. [CrossRef]

16. Otto, F.; Yang, Y.; Bei, H.; George, E.P. Relative effects of enthalpy and entropy on the phase stability of equiatomic high-entropy alloys. *Acta Mater.* **2013**, *61*, 2628–2638. [CrossRef]
17. Otto, F.; Dlouhý, A.; Pradeep, K.G.; Kuběnová, M.; Raabe, D.; Eggeler, G.; George, E.P. Decomposition of the single-phase high-entropy alloy CrMnFeCoNi after prolonged anneals at intermediate temperatures. *Acta Mater.* **2016**, *112*, 40–52. [CrossRef]
18. Bei, H. Multi-Component Solid Solution Alloys Having High Mixing Entropy. US Patent US9150945B2, 6 October 2015.
19. Senkov, O.N.; Wilks, G.B.; Miracle, D.B.; Chuang, C.P.; Liaw, P.K. Refractory high-entropy alloys. *Intermetallics* **2010**, *18*, 1758–1765. [CrossRef]
20. Senkov, O.N.; Wilks, G.B.; Scott, J.M.; Miracle, D.B. Mechanical properties of Nb25Mo25Ta 25W25 and V20Nb20Mo 20Ta20W20 refractory high entropy alloys. *Intermetallics* **2011**, *19*, 698–706. [CrossRef]
21. Materialprüfung, DIN-Normenausschuss. Gleitlager, DIN-Normenausschuss Wälz- und DIN 50106 Prüfung Metallischer Werkstoffe—Druckversuch bei Raumtemperatur. 2016. Available online: https://www.din.de/de/mitwirken/normenausschuesse/nawgl (accessed on 16 November 2020).
22. Hasegawa, M. *Thermodynamic Basis for Phase Diagrams*; Elsevier Ltd.: London, UK, 2013; Volume 1, ISBN 9780080969862.
23. Yang, X.; Zhang, Y. Prediction of high-entropy stabilized solid-solution in multi-component alloys. *Mater. Chem. Phys.* **2012**, *132*, 233–238. [CrossRef]
24. Fang, S.; Xiao, X.; Xia, L.; Li, W.; Dong, Y. Relationship between the widths of supercooled liquid regions and bond parameters of Mg-based bulk metallic glasses. *J. Non-Cryst. Solids* **2003**, *321*, 120–125. [CrossRef]
25. Kittel, C. *Introduction to Solid State Physics*, 8th ed.; Wiley John + Sons: Berkeley, CA, USA, 2008; ISBN 047141526X.
26. Zhang, Y.; Zhou, Y.J.; Lin, J.P.; Chen, G.L.; Liaw, P.K. Solid-solution phase formation rules for multi-component alloys. *Adv. Eng. Mater.* **2008**, *10*, 534–538. [CrossRef]
27. Zhang, Y.; Lu, Z.P.; Ma, S.G.; Liaw, P.K.; Tang, Z.; Cheng, Y.Q.; Gao, M.C. Guidelines in predicting phase formation of high-entropy alloys. *MRS Commun.* **2014**, *4*, 57–62. [CrossRef]
28. Wu, C.S.; Tsai, P.H.; Kuo, C.M.; Tsai, C.W. Effect of atomic size difference on the microstructure and mechanical properties of high-entropy alloys. *Entropy* **2018**, *20*, 967. [CrossRef]
29. Ye, Y.F.; Wang, Q.; Lu, J.; Liu, C.T.; Yang, Y. High-entropy alloy: Challenges and prospects. *Mater. Today* **2016**, *19*, 349–362. [CrossRef]
30. Becker, J.; Betke, U.; Wessel, E.; Krüger, M. Alloying effects in Mo-5X (X = Zr, Ti,V)—Microstructural modifications and mechanical properties. *Mater. Today Commun.* **2018**, *15*, 314–321. [CrossRef]
31. Sahm, P.R.; Egry, I.; Volkmann, T. *Schmelze, Erstarrung, Grenzflächen*; Sahm, P.R., Egry, I., Volkmann, T., Eds.; Springer Berlin Heidelberg: Berlin/Heidelberg, Germany, 1999; ISBN 978-3-540-41566-4.
32. Sheikh, S.; Shafeie, S.; Hu, Q.; Ahlström, J.; Persson, C.; Veselý, J.; Zýka, J.; Klement, U.; Guo, S. Alloy design for intrinsically ductile refractory high-entropy alloys. *J. Appl. Phys.* **2016**, *120*, 164902. [CrossRef]
33. Yao, H.; Qiao, J.W.; Gao, M.C.; Hawk, J.A.; Ma, S.G.; Zhou, H. MoNbTaV medium-entropy alloy. *Entropy* **2016**, *18*, 189. [CrossRef]
34. Yao, H.W.; Qiao, J.W.; Gao, M.C.; Hawk, J.A.; Ma, S.G.; Zhou, H.F.; Zhang, Y. NbTaV-(Ti,W) refractory high-entropy alloys: Experiments and modeling. *Mater. Sci. Eng. A* **2016**, *674*, 203–211. [CrossRef]
35. *Special Metals IN718 Datasheet*; Special Metals Corporation: New Hartford, NY, USA, 2007; Volume 75.
36. Sengupta, A.; Putatunda, S.K.; Bartosiewicz, L.; Hangas, J.; Nailos, P.J.; Peputapeck, M.; Alberts, F.E. Tensile behavior of a new single crystal nickel-based superalloy (CMSX-4) at room and elevated temperatures. *J. Mater. Eng. Perform.* **1994**, *3*, 664–672. [CrossRef]
37. Basak, A.; Holenarasipura Raghu, S.; Das, S. Microstructures and Microhardness Properties of CMSX-4® Additively Fabricated Through Scanning Laser Epitaxy (SLE). *J. Mater. Eng. Perform.* **2017**, *26*, 5877–5884. [CrossRef]
38. *HAYNES® 282® Alloy—Principal Features*; Haynes International: Kokomo, IN, USA, 2020.